



Cite this: *RSC Adv.*, 2022, **12**, 1244

## A minireview on catalysts for photocatalytic N<sub>2</sub> fixation to synthesize ammonia

Ping Qi,<sup>a</sup> Xiaoxu Gao,<sup>a</sup> Jian Wang,<sup>a</sup> Huimin Liu,<sup>a</sup> Dehua He<sup>b</sup> and Qijian Zhang<sup>a</sup>

Ammonia (NH<sub>3</sub>) is an important feedstock in chemical industry. Nowadays NH<sub>3</sub> is mainly produced via the industrialized Haber–Bosch process, which requires substantial energy input, since it operates at high temperatures (400–650 °C) and high pressures (20–40 Mpa). From the energy conservation point of view, it is of great significance to explore an alternative avenue to synthesize NH<sub>3</sub>, which is in line with the concept of sustainable development. Very recently, photocatalytic N<sub>2</sub> fixation (PNF) has been discovered as a safe and green approach to synthesize NH<sub>3</sub>, as it utilizes the inexhaustible solar energy and the abundant N<sub>2</sub> in nature to synthesize NH<sub>3</sub> under mild conditions. A highly efficient catalyst is the core of PNF. Up to now, extensive studies have been conducted to design efficient catalysts for PNF. Summarizing the catalysts reported for PNF and unraveling their reaction mechanisms could provide guidance for the design of better catalysts. In this review, we will illustrate the development of catalysts for PNF, including semiconductors, plasmonic metal-based catalysts, iron-based catalysts, ruthenium-based catalysts and several other catalysts, point out the remaining challenges and outline the future opportunities, with the aim to contribute to the development of PNF.

Received 1st November 2021  
 Accepted 16th December 2021

DOI: 10.1039/d1ra08002d

rsc.li/rsc-advances

### Introduction

Ammonia (NH<sub>3</sub>) is one of the basic raw materials in industrial chemistry and has been widely applied in various fields.<sup>1–4</sup>

<sup>a</sup>School of Chemical and Environmental Engineering, Liaoning University of Technology, Jinzhou 121001, P. R. China. E-mail: liuhuimin08@tsinghua.org.cn; zhangqijian@tsinghua.org.cn

<sup>b</sup>Innovative Catalysis Program, Key Lab of Organic Optoelectronics & Molecular Engineering of Ministry of Education, Department of Chemistry, Tsinghua University, Beijing 100084, P. R. China

Industrially, NH<sub>3</sub> could be used to produce fertilizers, synthetic fibres, nitrile rubber and so on; medically, NH<sub>3</sub> is often utilized as a drug to treat dizziness and fainting; militarily, NH<sub>3</sub> could serve as a biological disinfectant to disinfect sarin agents. The wide applications of NH<sub>3</sub> make it essential in promoting the development of national economies.

At present, the Haber–Bosch process is the main approach to synthesize NH<sub>3</sub>.<sup>5–8</sup> However, the Haber–Bosch process is carried out under harsh reaction conditions (the pressure is high up to 20–40 MPa and the temperature is in the range of 400–650 °C), which consumes extensive energy.<sup>9,10</sup> From the context of global



Ping Qi, lecturer, School of chemistry and environmental engineering, Liaoning University of Technology. 1993–1997, Fushun Petroleum Institute, petrochemical branch, undergraduate. 1997–2004, engineer, isopropanol workshop, Jinzhou Petrochemical Company. 2004–2007, Liaoning University of Technology, master, advisor: Qijian Zhang. 2007–present, lecturer, School of chemistry and environmental engineering, Liaoning University of Technology.



Huimin Liu received the Ph.D. degree from Tsinghua University, China (2013), and then joined Kansai University (2013–2014), National Institute of Materials Science (NIMS, 2014–2017) and the University of Sydney (2017–2019) as postdoctoral researcher and Lecturer. Now she is working in Liaoning University of Technology as a professor. Her research interests are photochemistry, environmental chemistry and heterogeneous catalyst design.



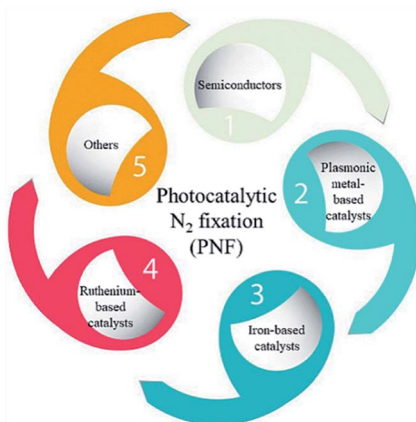


Fig. 1 Schematic illustration of catalysts that have been designed for PNF.

energy crisis, it is necessary to search for an alternative avenue to synthesize  $\text{NH}_3$  which is in line with the concept of sustainable development.

Photocatalytic  $\text{N}_2$  fixation (PNF) is a process which utilizes the inexhaustible solar energy and the abundant  $\text{N}_2$  in nature to synthesize  $\text{NH}_3$  under mild conditions.<sup>11–18</sup> It is a safe and green approach and has great potential to solve the problems encountered in the industrialized Haber-Bosch process, provided that efficient photocatalysts are adopted.<sup>19–31</sup>

In photocatalytic  $\text{N}_2$  fixation reaction, the cleavage of the  $\text{N}\equiv\text{N}$  bond is the rate determining step. That is, effective catalysts for PNF should be able to accelerate the  $\text{N}\equiv\text{N}$  bond cleavage process.

Over the past few years, an enormous amount of research effort has been devoted to explore effective catalysts for PNF. A large number of photocatalysts, such as semiconductors, plasmonic metal-based catalysts, iron-based catalysts, ruthenium-based catalysts and several other catalysts, have been designed for PNF (a schematic illustration is shown in Fig. 1).

For each type of these photocatalysts, a specific photocatalyst for PNF could be simply divided into two different functional units. One is the light harvesting unit (which is used to denote the active sites that could adsorb light) and the other is the



*Qijian Zhang received the Ph.D. degree from Tsinghua University, China (2003), and then joined the University of Kitakyushu for cooperative research (2003–2005). From 2003 to now, he is working in Liaoning University of Technology as a professor. His research interests are nano catalysis and energy chemistry, which is dimethyl ether reforming to hydrogen, application of nano Ni based catalyst in  $\text{CH}_4$  reforming, photo-thermal catalysis, etc.*

thermal-driven active unit (which is referred as the active center that directly involves in the polarization and activation of  $\text{N}_2$ ). The tailoring of each of the type of functional unit could contribute to the performance of a catalyst in PNF. In this review, we will summarize the photocatalysts that have been reported active for PNF, generalize the principles for the design of efficient catalysts (tailoring the light harvesting unit or the thermal-driven active unit), unravel their reaction mechanisms, point out the remaining challenges and prospect the future development, with the aim to provide guidance for the rational design of more efficient photocatalysts and contribute to the development of PNF.

## Photocatalysts for PNF

In this section, the photocatalysts for PNF are classified into five categories, including semiconductors, plasmonic metal-based catalysts, iron-based catalysts, ruthenium-based catalysts and other catalysts. The progress of each category of photocatalysts is summarized and discussed in the following sub-sections.

### Semiconductors as photocatalysts for PNF

When semiconductors are adopted to catalyse PNF, suitable energy band levels are required. Generally speaking, semiconductors for PNF are designed according to the following principles, ① the semiconductor could absorb light efficiently and it could be excited by light easily, ② the separation and transfer efficiency of the photogenerated electron hole pairs should be effective, and ③ the energy levels of the semiconductor photocatalyst could meet the standards for the two photo-induced half reactions, referring to the reduction of  $\text{N}_2$  and the oxidation of  $\text{H}_2$  or  $\text{H}_2\text{O}$ .

Some pristine semiconductors could meet the standards to drive PNF, however, their efficiencies are quite low. Introducing vacancies or foreign elements into the semiconductor, functionalizing the pristine semiconductor, constructing heterojunctions/homojunctions or design a semiconductor-based hydrophilic-hydrophobic catalyst, are approaches to extend the light harvesting spectrum, enhance the light harvesting capacity (which means its capacity to absorb more light), facilitate the separation and transfer of photoinduced electron hole pairs and further accelerate PNF.

**Pristine semiconductors.** Pristine semiconductors are a type of photocatalyst with only light harvesting unit for PNF. Pristine semiconductors are widely studied in PNF. The catalytic performance of pristine semiconductors could be improved by regulating their optical properties. Theoretical calculations suggest that (110) facet of rutile  $\text{TiO}_2$  is capable of activating  $\text{N}_2$  into  $\text{NH}_3$  via both the associative and dissociative mechanism;<sup>32</sup> (040) facet of  $\text{BiVO}_4$  single crystal could catalyze PNF, with  $\text{V}^{4+}/\text{V}^{5+}$  as the active site, where  $\text{V}^{4+}$  chemisorbs  $\text{N}_2$ ,  $\text{V}^{5+}$  serves as the electron transfer bridge and the photogenerated electrons are the driving force for PNF.<sup>33</sup>

The activities of pristine semiconductors have been verified experimentally. For example, ultrathin  $\text{MoS}_2$  could convert  $\text{N}_2$  into  $\text{NH}_3$  via a six-electron reduction process (Fig. 2), achieving



a  $\text{NH}_3$  synthesis rate of  $325 \mu\text{mol g}^{-1} \text{h}^{-1}$  without any sacrificial reagents or co-catalysts.<sup>34</sup> The electron-rich property of ultrathin  $\text{MoS}_2$  as well as the high concentration of localized electrons upon light irradiation accounted for its activity.<sup>34</sup> Bismuth monoxide ( $\text{BiO}$ ) quantum dots, synthesized *via* a facile hydrothermal method, are reported as a highly efficient catalyst for PNF, recording a  $\text{NH}_3$  generation rate of  $1226 \mu\text{mol g}^{-1} \text{h}^{-1}$  without the assistance of any sacrificial reagents or co-catalysts.<sup>35</sup> It is postulated that all the low valence  $\text{Bi}(\text{II})$  in  $\text{BiO}$  were potential active sites for  $\text{N}_2$  activation.<sup>35</sup>

The catalytic activity of pristine semiconductor could be improved, in case that a 2-dimensional (2D) material is used as co-catalyst. For instance, P25 itself yielded  $\text{NH}_3$  at a rate of  $2.11 \mu\text{mol g}^{-1} \text{h}^{-1}$  under full spectrum light irradiation, while the activity was fivefold increased when  $\text{Ti}_3\text{C}_2$  MXene was used as a co-catalyst.<sup>36</sup> Similarly, the catalytic performance of  $\text{CdS}$  in PNF boosted obviously when black phosphorous nanosheet was adopted as a co-catalyst.<sup>37</sup> It is reported that 2D co-catalysts facilitated the separation of electron-hole pairs and promoted  $\text{N}_2$  chemisorption and activation.

Despite that some pristine semiconductors are active for PNF, their efficiencies are generally low. To further improve their efficiencies, multiple approaches are adopted to modify the pristine semiconductors.

**Semiconductors with vacancies.** Introducing vacancies into a semiconductor endows the pristine semiconductor additional properties. On one hand, vacancy introduction could tailor the light harvesting unit of the photocatalyst, such as narrow its band gap, extend its light harvesting range and enhance its light harvesting capacity. On the other hand, the vacancies occasionally serve as thermal-driven active sites for  $\text{N}_2$  activation. Defective semiconductors have been widely applied in PNF. The functions of the defective sites vary with the catalytic systems.

(1) The introduction of defective sites engineers the light harvesting unit, such as lowers the conduction band position, engineers the band gap and improves the light harvesting capacity of the semiconductor. Few-layer  $\text{g-C}_3\text{N}_4$  (ref. 38) and one-dimensional  $\text{g-C}_3\text{N}_4$  (ref. 39) are rich in N defects. The existence of N defective sites lowered the conduction band position and increased its light harvesting capacity, which then contribute to their performance in PNF.<sup>38,39</sup> Band gaps and the light harvesting capacities could be consecutively tuned by dedicatedly controlling the content of surface vacancies.<sup>40</sup>

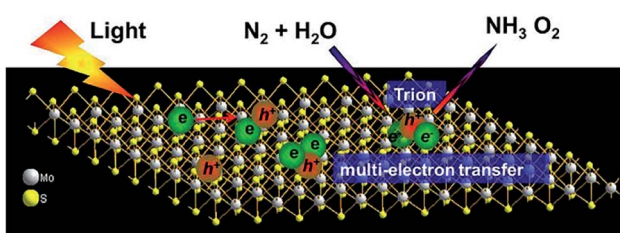


Fig. 2 Schematic illustration of trion induced six-electron  $\text{N}_2$  reduction. This figure has been adapted from ref. 34 with permission from Elsevier, copyright 2017.

(2) The defective sites serve as the active sites to enhance the adsorption and activation of  $\text{N}_2$ . N vacancies on nitrides generally activate  $\text{N}_2$  *via* a pathway analogous to Mar-van Krevelen mechanism. That is,  $\text{N}_2$  is firstly activated at the N vacancies and then transformed into  $\text{NH}_3$  by reacting with  $\text{H}_2$  or  $\text{H}_2\text{O}$ . Wang *et al.*'s work is a typical example. In their work, a N deficient  $\text{g-C}_3\text{N}_4$  catalyst was prepared by the dielectric barrier discharge plasma treatment method, which displayed a  $\text{NH}_3$  production rate of  $161.8 \mu\text{mol g}^{-1} \text{h}^{-1}$ .<sup>41</sup> Mechanism exploration disclosed that  $\text{N}_2$  was activated *via* the two-path analogous Mar-van Krevelen mechanism.<sup>41</sup>

Oxygen vacancies on oxide semiconductors are active centers for  $\text{N}_2$  adsorption and capable of activating  $\text{N}_2$ .<sup>42-44</sup> Theoretical study revealed that the oxygen vacancies on (001) and (100) facets of  $\text{MoO}_{3-x}$  nanobelts could chemisorb  $\text{N}_2$  *via* side-on and end-on models, respectively, which accelerates the sluggish rate determining step ( $\text{N}_2$  activation) in PNF and boosted its performance.<sup>43</sup>

Cation defective sites on a semiconductor are electron-rich, which could effectively activate the  $\text{N}\equiv\text{N}$  bond and accelerate catalytic activity in PNF. For instance, Zn deficient  $\text{Zn}_3\text{In}_2\text{S}_6$  exhibited a  $\text{NH}_3$  generation rate of  $261.2 \mu\text{mol g}^{-1} \text{h}^{-1}$  under visible light irradiation, 15 times higher than the one with poor defects.<sup>45</sup>

(3) On some defective semiconductors, the defective sites not only improve light harvesting capacity but also facilitate  $\text{N}_2$  activation. For example,  $\text{Bi}_2\text{WO}_6$  hollow microspheres prepared by a solvothermal template-free method are rich in oxygen vacancies.<sup>46</sup> The oxygen vacancies induce a sub-band (defect energy level), which not only narrows its band gap and extends its light absorption region (up to 700 nm), but also localizes metastable electrons. These metastable electrons jump to the anti-bonding orbitals of  $\text{N}_2$  *via* a manner of non-radiative transfer and activate  $\text{N}_2$ . Overall, the  $\text{Bi}_2\text{WO}_6$  hollow microspheres demonstrated a  $\text{NH}_3$  yield of  $\sim 53 \mu\text{mol g}^{-1} \text{h}^{-1}$  under simulated sunlight.<sup>46</sup>

Similarly, in addition to enhance the light harvesting capacity, the oxygen vacancies on  $\text{BiOCl}$ ,<sup>47</sup>  $\text{TiO}_2$ ,<sup>48-50</sup> and  $\text{BiOBr}$ <sup>51</sup> also serve as the active sites for  $\text{N}_2$  activation and reduction while the oxygen vacancies on  $\text{Bi}_3\text{FeMo}_2\text{O}_{12}$  help adsorb and stabilize the N-H intermediate during  $\text{N}_2$  activation,<sup>52</sup> which cooperatively boost  $\text{NH}_3$  production *via* PNF (Fig. 3).<sup>53</sup>

Intrinsic strain is occasionally induced by vacancies. Thereby the strain and vacancies cooperatively contribute to PNF. Zhang *et al.* synthesized an ultrathin  $\text{TiO}_2$  nanosheet catalyst with

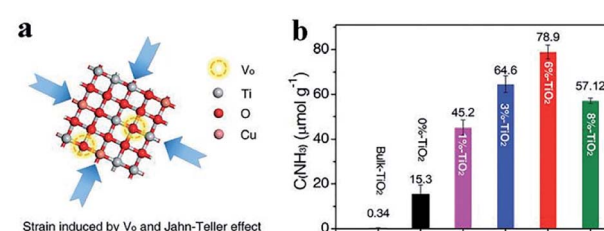


Fig. 3 (a) Strain induced by oxygen vacancies and Jahn-Teller effects in  $\text{TiO}_2$  nanosheet. (b)  $\text{NH}_3$  yield over different catalysts under ultraviolet (UV)-vis light irradiation for 1 h. This figure has been adapted from ref. 53 with permission from Wiley-VCH, copyright 2019.



abundant oxygen vacancies *via* a facile copper-doping method, which could absorb visible light high up to 700 nm.<sup>53</sup> It was discovered that there was intrinsic compression strain in the as-prepared  $\text{TiO}_2$  nanosheet. The oxygen vacancies and the strain worked in concert to chemisorb and activate  $\text{N}_2$  and  $\text{H}_2\text{O}$  effectively, leading to a high  $\text{NH}_3$  production rate ( $78.9 \mu\text{mol g}^{-1} \text{h}^{-1}$ ).<sup>53</sup>

**Doped semiconductors.** Doping one or more foreign elements into a semiconductor is an important approach to mediate the light harvesting unit (such as introduce new energy levels, engineer its energy structure, tailor its light harvesting capacity) and/or manipulate the active sites for  $\text{N}_2$  activation. Doped semiconductor is a category of catalysts for PNF. Here, based on the functions of the dopant, the doped semiconductor catalyst for PNF is review.

(1) Suitable dopant could serve as active sites for promoting  $\text{N}_2$  activation. For example,  $\text{Mo}_{1-x}\text{W}_x\text{S}_2$  nanosheets, which could be considered as Mo doped  $\text{WS}_2$ , recorded a  $\text{NH}_3$  production rate of  $111 \mu\text{mol g}^{-1} \text{h}^{-1}$  under visible light irradiation, when the concentration of 1T phase was 33.6% and  $\text{Mo/W} = 0.68 : 0.32$ .<sup>54</sup> The doping of Mo into  $\text{WS}_2$  resulted in a higher electron density on W 5d orbitals, which polarized the adsorbed  $\text{N}_2$  and responded for its PNF activity.<sup>54</sup>

(2) Under most of cases, the introduction of dopant not only engineers the optical properties but also manipulates the active sites for  $\text{N}_2$  activation.

Doping B into  $\text{g-C}_3\text{N}_4$  led to the formation of a new chemical bond B–N–C, which not only effectively enhanced the light harvesting capacity and suppressed the recombination of photoinduced electron–hole pairs, but also served as an active center for  $\text{N}_2$  chemisorption and activation.<sup>55</sup> In the issue, B- $\text{g-C}_3\text{N}_4$  gave a  $\text{NH}_3$  yield of  $313.9 \mu\text{mol g}^{-1} \text{h}^{-1}$  under visible light assistance.<sup>55</sup>  $\text{Mn}^{2+}$  could be doped into  $\text{W}_{18}\text{O}_{49}$  *via* partially replacing the W sites.<sup>56</sup> The doped  $\text{Mn}^{2+}$  played multiple roles in PNF. ①  $\text{Mn}^{2+}$  acted as the active sites for the chemisorption of  $\text{N}_2$  and  $\text{H}_2\text{O}$ , ②  $\text{Mn}^{2+}$  weakened the  $\text{N}\equiv\text{N}$  bond through proton coupling process and ③ the doped  $\text{Mn}^{2+}$  facilitated the separation and migration of photoinduced electron–hole pairs. Based on these advantages, the as prepared  $\text{Mn-W}_{18}\text{O}_{49}$  catalyst exhibited a  $\text{NH}_3$  production rate of  $97.9 \mu\text{mol g}^{-1} \text{h}^{-1}$  under full spectrum irradiation of a 300 W Xe lamp.<sup>56</sup>

When a foreign element is doped into a semiconductor with vacancies sites, the dopants and vacancies sites might synergistically activate  $\text{N}_2$  and contribute to PNF. For example, in sulfur doped oxygen deficient  $\text{TiO}_2$  ( $\text{TiO}_{2-x}\text{S}_y$ ), the oxygen vacancies and sulfur dopant worked in concert to facilitate  $\text{N}_2$  adsorption and extend its light absorbing capacity to near-infrared region.<sup>57</sup> As a result,  $\text{TiO}_{2-x}\text{S}_y$  yielded  $\text{NH}_3$  at a rate of  $114.1 \mu\text{mol g}^{-1} \text{h}^{-1}$  under full spectrum light irradiation.<sup>57</sup> Similar phenomena were also observed over Br doped  $\text{BiOCl}$  with oxygen vacancies,<sup>58</sup> Ni doped vacancy-rich  $\text{TiO}_2$ ,<sup>59</sup> as well as S doped  $\text{g-C}_3\text{N}_4$  with carbon vacancies.<sup>60</sup>

Doping a foreign element into a semiconductor sometimes leads to the generation of vacancies. Tang *et al.* fabricated a carbon doped  $\text{TiO}_2$  nanosheet catalyst (C-TiOx) from  $\text{Ti}_3\text{SiC}_2$  *via* a bottom-up approach (Fig. 4a).<sup>29</sup> It was discovered that the doping of carbon led to the generation of oxygen vacancies in  $\text{TiO}_2$ . As charge compensation, controllable  $\text{Ti}^{3+}$  sites were

produced. The oxygen vacancies broadened its light harvesting region and the electron-rich  $\text{Ti}^{3+}$  were active for  $\text{N}_2$  activation. With Ru/RuO<sub>2</sub> as co-catalyst to promote the separation and migration of photoinduced electron–hole pairs, the optimal C-TiO<sub>x</sub> recorded a  $109.3 \mu\text{mol g}^{-1} \text{h}^{-1}$   $\text{NH}_3$  synthesis rate under visible light irradiation and an apparent quantum yield of 1.1% at 400 nm (Fig. 4b).<sup>29</sup> Similarly, oxygen vacancies could also be generated by doping carbon into  $\text{BiOI}$ .<sup>61</sup> Carbon dopant decreased the band gap, extended the light harvesting region, facilitated the separation and migration of electron–hole pairs and consequently hastened PNF, leading to a  $\text{NH}_3$  generation rate of  $311 \mu\text{mol g}^{-1} \text{h}^{-1}$  under the illumination of simulated sunlight.<sup>61</sup>

As for doping, it is clear that most of the doped semiconductors exhibited a  $\text{NH}_3$  production rate of  $\sim 100 \mu\text{mol g}^{-1} \text{h}^{-1}$ , with only two exceptions on B-g-C<sub>3</sub>N<sub>4</sub> and C-BiOI, who gave  $\text{NH}_3$  yields over  $300 \mu\text{mol g}^{-1} \text{h}^{-1}$ . Even though limited by the number of studies, it might provide a clue that nonmetal element doping could endow the doped semiconductors better performance in PNF.

**Functionalized semiconductors.** Grafting functional groups onto a semiconductor or modifying a pristine semiconductor is an important approach to mediate the two functional units and consequently enhance their performance for PNF.

(1) Functionalized semiconductors with engineered light harvesting unit.

Acid treated semiconductors. Tian *et al.* reported that salicylic acid (SA) modification could enlarge the Brunauer–Emmett–Teller surface area, improve the optical absorption capacity as well as promote the separation of photoinduced electron–hole pairs in  $\text{g-C}_3\text{N}_4$ , which resulted in a much enhanced PNF activity over  $\text{g-C}_3\text{N}_4\text{-SA}$ .<sup>62</sup>

Base treated semiconductors. It has been reported that base treated semiconductors exhibited improved electron–hole separation efficiency. Typical examples are given by Yangjeh *et al.*<sup>63</sup> and Wang *et al.*,<sup>64</sup> who reported that MgO decorated  $\text{g-C}_3\text{N}_4$  and KOH treated  $\text{g-C}_3\text{N}_4$  gave superior performance in PNF than pristine  $\text{g-C}_3\text{N}_4$ , and the reduced recombination rate of electron–hole pairs was one of the reasons for their premier activities.

Metal decorated semiconductors. Cu, Fe, Ni and Pd decoration could promote the charge transfer efficiency. Cu, Fe or Ni decorated  $\text{TiO}_2$ , synthesized *via* microwave assisted hydro-thermal method, not only exhibited promoted charge transfer efficiency, but also had larger specific surface area and stronger capacity in harvesting visible light.<sup>65</sup> As a result, they exhibited 1.9–6.0 times higher PNF activities than the pristine  $\text{TiO}_2$  under simulated light irradiation.<sup>65</sup> Pd decorated  $\text{TiO}_2$ , prepared by one-pot microwave synthesis techniques, also demonstrated reduced recombination of photoinduced electron–hole pairs and led to a 4 fold higher  $\text{NH}_3$  production rate than the unmodified one.<sup>66</sup>

Quantum dots modified semiconductors. Graphene quantum dots modified  $\text{Bi}_2\text{WO}_6$ , with graphene quantum dots uniformly dispersed on the surface of  $\text{Bi}_2\text{WO}_6$ , exhibited remarkably enhanced PNF activity than the two single component counterparts. Characterization results implied that the recombination of photoinduced electron–hole pairs was



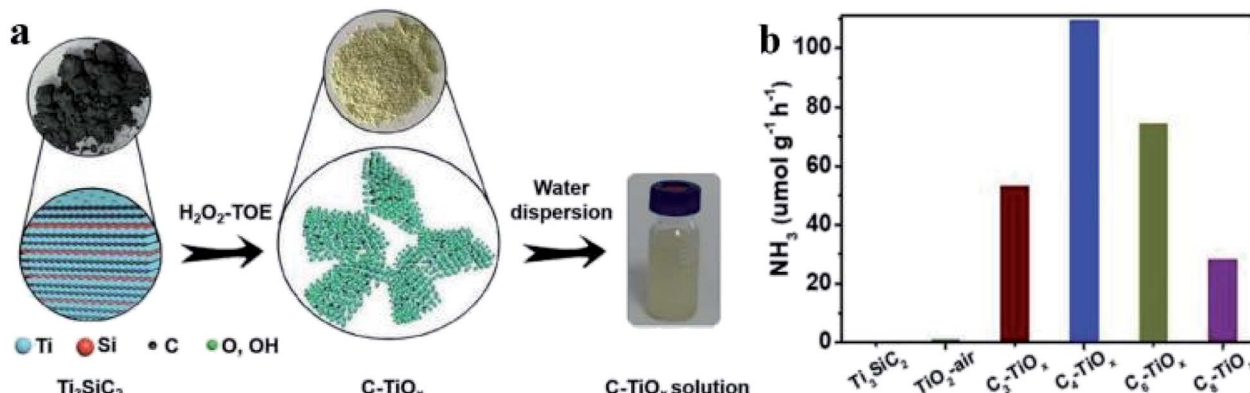


Fig. 4 (a) Schematic illustration for the synthesis of C-TiO<sub>x</sub>. (b) Photocatalytic performance of C<sub>n</sub>-TiO<sub>x</sub> (n denotes the treatment time of Ti<sub>3</sub>SiC<sub>2</sub>) and Ti<sub>3</sub>SiC<sub>2</sub> in PNF under visible light irradiation. Ru/RuO<sub>2</sub> was used as co-catalyst. This figure has been adapted from ref. 29 with permission from Wiley-VCH, copyright 2021.

significantly reduced and the junction between graphene quantum dots and Bi<sub>2</sub>WO<sub>6</sub> helped to boost the photocatalytic activity.<sup>67</sup>

## (2) Functionalized semiconductors with tailored active sites.

**Hydrogenated semiconductors.** Unsaturated Mo atoms in Bi<sub>2</sub>MoO<sub>6</sub> are the active sites for N<sub>2</sub> chemisorption, activation and reduction, on the contrary, the Mo atoms within the crystal are always inert. Focusing on this standpoint, Zhang *et al.* hydrogenated Bi<sub>2</sub>MoO<sub>6</sub> with the aim to expose more unsaturated Mo atoms by inducing the escape of oxygen atoms in saturated Mo-O bond and enhance its N<sub>2</sub> activation capacity. As expected, the hydrogenated Bi<sub>2</sub>MoO<sub>6</sub> exhibited a NH<sub>3</sub> production rate 9.5 times higher than that of untreated one, up to 1.3 mmol g<sup>-1</sup> h<sup>-1</sup>.<sup>68</sup>

(3) Functionalized semiconductors with two functional units modified.

**Semiconductors with functional groups.** Grafting amine groups onto g-C<sub>3</sub>N<sub>4</sub> could enhance the charge separation efficiency and consequently nearly double its activity in PNF.<sup>69</sup> Introducing cyano groups onto g-C<sub>3</sub>N<sub>4</sub> not only improves the separation and migration of photoinduced electron-hole pairs but also enhances N<sub>2</sub> activation owing to its electron-withdrawing characteristics. Thus, cyano group functionalized g-C<sub>3</sub>N<sub>4</sub> resulted in a 12.8 times promoted activity in PNF than pristine g-C<sub>3</sub>N<sub>4</sub>.<sup>70</sup> With the assistance of K, the cyano group on modified g-C<sub>3</sub>N<sub>4</sub> could be regenerated readily *via* the analogous Mars van Krevelen mechanism, which ensured the stability of the functionalized semiconductors.<sup>12</sup>

**Hydrogenated semiconductors.** Dong *et al.* reported that hydrogen treatment could withdraw the oxygen atoms and leave oxygen vacancies in BiOBr, which then broadened the photoelectricity absorption window, triggered the electron transfer from BiOBr to the adsorbed N<sub>2</sub>, and responded for the 2.6 times improved PNF efficiency, compared to the untreated counterpart.<sup>71</sup>

**Acid treated semiconductors.** Wang *et al.* reported that phosphate acid treated LaFeO<sub>3</sub> could catalyze PNF effectively, producing NH<sub>3</sub> at a rate of ~250 μmol g<sup>-1</sup> h<sup>-1</sup> under simulated

light irradiation. Mechanism exploration suggested that phosphate acid served as the Lewis acid center, it worked synergistically with Fe in LaFeO<sub>3</sub> to activate N<sub>2</sub> *via* the “push-pull” hypothesis. That is, the electron density is pulled from Fe and pushed into N<sub>2</sub> by the adjacent hydrogen bonding sites. In addition, phosphate modification facilitated H<sub>2</sub>O dissociation.<sup>72</sup>

**Metal decorated semiconductors.** In case that a metal is decorated onto a semiconductor with vacancy sites, the doped metal and the vacancies work in concert to promote N<sub>2</sub> activation. For instance, Dong *et al.* constructed a Bi/BiOBr heterostructure with abundant oxygen vacancies *via* a one-step solvothermal strategy. In BiOBr, the oxygen defective sites were the active centers for N<sub>2</sub> adsorption. Bi and oxygen vacancies promoted the interfacial charge transfer from Bi/BiOBr to the adsorbed N<sub>2</sub>, facilitated charge separation efficiency and accounted for a remarkably high NH<sub>3</sub> production rate (1350 μmol g<sup>-1</sup> h<sup>-1</sup>).<sup>73</sup>

**Heterojunctions and homojunctions.** Heterojunctions and homojunctions are fabricated by integrating two or more semiconductors. Heterojunctions and homojunctions generally inherit the merits of each single semiconductor counterpart, exhibit stronger light harvesting capacities and deliver high photocatalytic activities. Further introducing other dopants or vacancies into heterojunctions or homojunctions might tailor the active centers for N<sub>2</sub> activation. The advantages of heterojunctions and homojunctions make them applicable in PNF.

(1) Heterojunctions/homojunctions with modified light harvesting unit. Bi<sub>2</sub>Te<sub>3</sub>/BiOCl,<sup>74</sup> g-C<sub>3</sub>N<sub>4</sub>/ZrO<sub>2</sub>,<sup>75</sup> MoO<sub>2</sub>/BiOCl<sup>76</sup> perovskite/attapulgite<sup>77</sup> and CdS/LDH (LDH: layered double hydroxide)<sup>78</sup> are typical heterojunctions that have been reported active in PNF. Here CdS/LDH is taken as an example for elaboration. In the case that CdS/LDH heterojunction was constructed between (003) or (012) facet of LDH and (002) facet of CdS, a build-in electric field would be induced under light irradiation, which promoted charge transfer from the heterostructure to the reaction media for N<sub>2</sub> activation *via* a favorable configuration and resulted in a better catalytic activity.<sup>78</sup>



Z scheme is a special case of heterojunctions. Z schemes AgBr/Bi<sub>4</sub>O<sub>5</sub>Br<sub>2</sub>,<sup>79</sup> Bi<sub>2</sub>O<sub>3</sub>@CoAl-LDHs,<sup>80</sup> 3,4-dihydroxybenzaldehyde-functionalized Ga<sub>2</sub>O<sub>3</sub>/g-C<sub>3</sub>N<sub>4</sub>,<sup>81</sup> g-C<sub>3</sub>N<sub>4</sub>/Mg<sub>1.1</sub>Al<sub>0.3</sub>Fe<sub>0.2</sub>O<sub>1.7</sub>,<sup>82</sup> nano-MOF@defected g-C<sub>3</sub>N<sub>4</sub> (MOF: metal organic frameworks)<sup>83</sup> and SiW<sub>9</sub>Co<sub>3</sub>/PDA/BWO (PDA: poly-dopamine; BWO: Bi<sub>2</sub>WO<sub>6</sub>)<sup>84</sup> have been reported active in PNF. In these Z schemes, the separation of photoinduced electron–hole pairs was significantly improved, which played a dispensable role in boosting their catalytic activities.

(2) Heterojunctions/homojunctions with modified light harvesting unit and active sites.

The catalytic activities of heterojunctions in PNF could be further improved by doping foreign elements, introducing defective sites or loading another component to one of the semiconductors of heterojunctions. N deficient g-C<sub>3</sub>N<sub>4</sub>/Cu<sub>2</sub>(OH)<sub>2</sub>CO<sub>3</sub>,<sup>85</sup> N deficient g-C<sub>3</sub>N<sub>4</sub>/Ag<sub>2</sub>CO<sub>3</sub>,<sup>86</sup> Bi<sub>2</sub>MoO<sub>6</sub>/oxygen-vacancy-rich BiOBr,<sup>87</sup> MoS<sub>2</sub>/C-ZnO (C was loaded onto ZnO),<sup>88</sup> TiO<sub>2</sub>@C g-C<sub>3</sub>N<sub>4</sub>,<sup>89</sup> B doped g-C<sub>3</sub>N<sub>4</sub>/Ni<sub>2</sub>P<sup>90</sup> and In<sub>2</sub>O<sub>3</sub>/In<sub>2</sub>S<sub>3</sub> (oxygen vacancies are generated *in situ*)<sup>91</sup> are representatives. In this type of heterojunctions, the junctions between the two semiconductors as well as the doped/loaded component or defective sites synergistically contributed to their activities in PNF.

Homojunction catalyst such as ordered/disordered TiO<sub>2</sub> exhibited a superior activity in PNF, affording a NH<sub>3</sub> formation rate of 432 μmol g<sup>-1</sup> h<sup>-1</sup> under solar illumination.<sup>92</sup> In the homojunction catalyst, ordered TiO<sub>2</sub> exhibited a stronger N<sub>2</sub> adsorption capacity with a reduced activation barrier while the disordered TiO<sub>2</sub> was rich in oxygen vacancies which selectively chemisorbed N<sub>2</sub> and enhanced visible light harvesting. The synergistic effect between ordered TiO<sub>2</sub> and disordered TiO<sub>2</sub>, together with the rapid interfacial charge separation, ensured its superior activity (Fig. 5).<sup>92</sup>

**Semiconductor-based hydrophilic-hydrophobic catalyst.** In case that H<sub>2</sub>O is the proton donor and solid catalyst is designed, PNF occurs at the gas (N<sub>2</sub>)-liquid (H<sub>2</sub>O)-solid (catalyst) triphase

interface. The poor solubility and the poor diffusion rate of N<sub>2</sub> in H<sub>2</sub>O severely limit the N<sub>2</sub> fixation efficiency. In order to overcome this obstacle, Fan *et al.* designed a Bi<sub>4</sub>O<sub>5</sub>Br<sub>2</sub>/ZIF-8 catalyst (ZIF-8 is a kind of MOFs), where Bi<sub>4</sub>O<sub>5</sub>Br<sub>2</sub> is hydrophilic whereas ZIF-8 is hydrophobic.<sup>93</sup> Such a hydrophilic–hydrophobic catalyst allowed the direct delivery of N<sub>2</sub> and H<sub>2</sub>O into the reaction interface, without the diffusion of N<sub>2</sub> in H<sub>2</sub>O. The rapid supply of N<sub>2</sub> ensured the efficient utilization of photoinduced electrons and led to a superior activity (NH<sub>3</sub> production rate was high up to 327 μmol g<sup>-1</sup> h<sup>-1</sup>).<sup>93</sup>

### Plasmonic metal-based catalysts for PNF

Plasmonic metals, such as Au and Ag, exhibit localized surface plasmon resonance (LSPR) effect upon light irradiation. The LSPR effects empower the plasmonic metal-based catalysts applicability in PNF. Over most of the plasmonic metal-based catalysts, the light harvesting unit and the active center work synergistically for improved performance. As the particle sizes, morphologies as well as the particle–particle distances of plasmonic metals are crucial for their light harvesting capacities, the tailoring of these properties are generally adopted with the aim to accelerate the reaction rate of plasmonic metal-based catalysts in PNF.

For example, Wang *et al.* encapsulated Au nanoparticles into a MOF membrane (UiO-66) and realized a NH<sub>3</sub> production rate of 359.1 μmol g<sup>-1</sup> h<sup>-1</sup> under visible light irradiation ( $\lambda > 400$  nm, 100 mW cm<sup>-2</sup>).<sup>94</sup> It was discovered that N<sub>2</sub> adsorbed on Au nanoparticles. Upon light irradiation, hot electrons generated on Au nanoparticles. The hot electrons on Au activated N<sub>2</sub> *via* two pathways, ① induced an electromagnetic field to polarize N<sub>2</sub> and ② directly injected into the anti-bonding orbitals of N<sub>2</sub> molecules (Fig. 6a). Moreover, the gas permeable nature of MOF membrane facilitated the mass transfer of the reactants, which further boosted its photocatalytic activity at

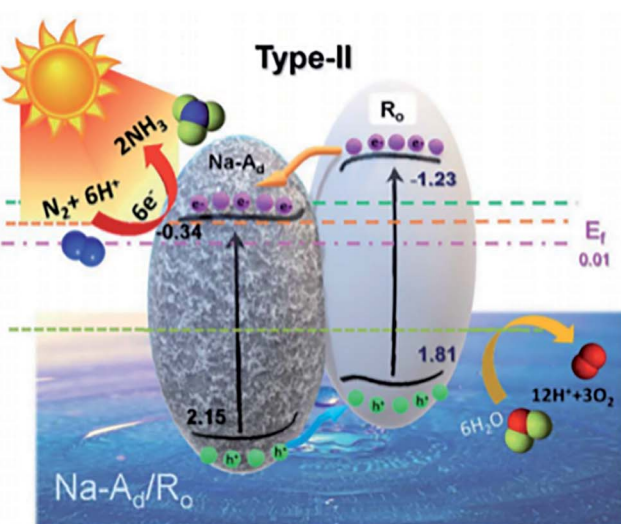
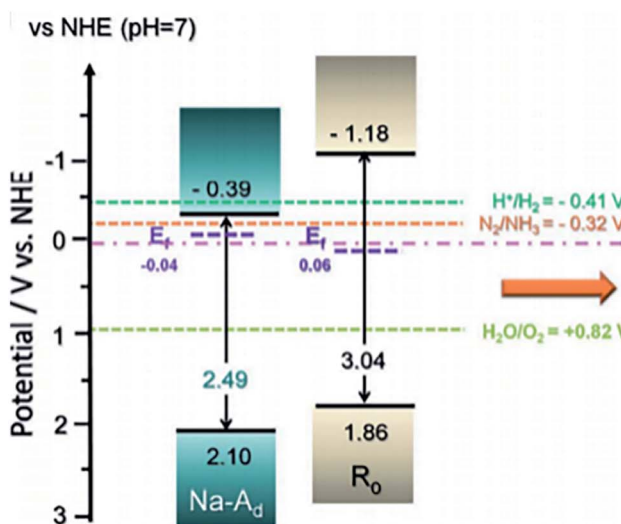


Fig. 5 Energy band structure of disordered TiO<sub>2</sub> (short for Na-Ad) and ordered TiO<sub>2</sub> (represented by R<sub>o</sub>) as well as the reaction mechanism. This figure has been adapted from ref. 92 with permission from Royal Society of Chemistry, copyright 2020.



the gas ( $N_2$ )-membrane (UiO-66 encapsulated Au nanoparticles)-solution ( $H_2O$ ) interface (Fig. 6b).<sup>94</sup>

Yang *et al.* reported that Au nanoparticles supported on nitrogen deficient g-C<sub>3</sub>N<sub>4</sub> could catalyze PNF, achieving a  $NH_3$  production rate of  $\sim 783 \mu\text{mol g}^{-1} \text{h}^{-1}$  under visible light irradiation.<sup>95</sup> In this catalytic system, the nitrogen vacancy sites adsorbed  $N_2$ ; Au and g-C<sub>3</sub>N<sub>4</sub> harvested visible light and induced electrons upon light irradiation, which then injected into  $N_2$  for its activation.<sup>95</sup> Liao *et al.* synthesized small Ag doped g-C<sub>3</sub>N<sub>4</sub> catalyst and unraveled that Ag enhanced  $N_2$  adsorption, generated more electrons, facilitated the separation and migration of photogenerated electron-hole pairs and consequently resulted in high activity in PNF.<sup>96</sup> Wang *et al.* supported Au nanocrystals onto Mo doped W<sub>18</sub>O<sub>49</sub> and realized a  $NH_3$  synthesis rate of  $\sim 399 \mu\text{mol g}^{-1} \text{h}^{-1}$ .<sup>97</sup> Au not only harvested visible light but also decreased the desorption energy of the product  $NH_3$ , which accelerated the regeneration of the active sites for next catalytic cycle.<sup>97</sup> Introducing a moderate amount of alkali metal cations could further promote  $N_2$  activation and then enhance the performance of these plasmonic metal-based catalysts in PNF.<sup>98</sup>

### Iron-based catalysts for PNF

Iron is the most active metal for  $N_2$  activation. The strong  $N_2$  activation capacity of iron makes it applicable as active center for PNF. However, the light harvesting capacity of iron is very weak. Integrating iron with a material that could harvest light efficiently is an approach to design the photocatalyst for PNF. Based on this principle, doping iron into semiconductors, loading iron onto semiconductors, constructing a Fe-based heterostructure catalyst and loading iron onto other light harvesting materials are promising avenues. Therefore, over most of the iron-based catalysts for PNF, both the light harvesting unit and the active center are regulated. Up to now, various iron-based catalysts have been designed. In this section, we will discuss the types of iron-based catalysts for PNF and emphasize their progress.

(1) Fe doped into semiconductors. Doping Fe into a semiconductor could tune the local electronic structure of the

catalysts and thereby facilitate  $N_2$  activation. For example, when Fe is doped into TiO<sub>2</sub>, Fe will substitute Ti atoms in TiO<sub>2</sub> owing to their similar radii, which creates oxygen vacancies at the neighbor of Fe atoms to meet the local charge balance.<sup>99</sup> The Fe atoms and oxygen vacancies work in concert to facilitate  $N_2$  adsorption and polarization, which enables  $N_2$  hydrogenation *via* the favorable associative distal pathway and contributes to PNF. As shown in Fig. 7a and b, 5wt% Fe/TiO<sub>2</sub> (5-FTNFs) afforded a stable  $NH_3$  production rate of  $\sim 64 \mu\text{mol g}^{-1} \text{h}^{-1}$  under the full spectrum illumination of a 300 W Xe lamp.<sup>99</sup> Isotope labeling experiment as well as <sup>1</sup>H-NMR (NMR: Nuclear magnetic resonance, Fig. 7c and d) indicated that the generated  $NH_3$  was originated from  $N_2$  instead of other contaminants.<sup>99</sup> Similarly, Fe-doped BiOBr with oxygen vacancies afforded a  $NH_3$  yield of  $46.1 \mu\text{mol g}^{-1} \text{h}^{-1}$  without any sacrificial reagent under  $400 \text{ mW cm}^{-2}$  visible light irradiation.<sup>100</sup> The doped Fe and the oxygen vacancies synergistically modulated the band structure, improved charge transfer and thereby enhanced the photocatalytic activities.<sup>100</sup>

Doping exerts functions beyond creating oxygen vacancies. For instance, the Fe atoms on the surface of Fe doped SrTiO<sub>3</sub> (Fe<sub>x</sub>Sr<sub>1-x</sub>TiO<sub>3</sub>) could not only chemisorb and activate  $N_2$ , but also promote the electron transfer from Fe<sub>x</sub>Sr<sub>1-x</sub>TiO<sub>3</sub> to  $N_2$ , which resulted in high  $N_2$  fixation capacity and a  $NH_3$  production rate of  $30.1 \mu\text{mol g}^{-1} \text{h}^{-1}$  over Fe<sub>x</sub>Sr<sub>1-x</sub>TiO<sub>3</sub> ( $x = 0.1$ ) under Xe lamp illumination.<sup>101</sup> Doping Fe into Mo-based semiconductors could narrow their band gaps, extend their light absorption capacities as well as generate new Fe-Mo active centers, which enables Fe doped Mo-based semiconductor to harvest more solar light and facilitate the electron-hole separation and migration efficiency.<sup>102</sup> Chang *et al.* doped Fe into 2D MoTe<sub>2</sub> nanosheets to construct Fe-Mo active centers.<sup>103</sup> It is reported that Fe doped into MoTe<sub>2</sub> facilitated the separation and transfer of photoinduced electron-hole pairs, prolonged their lifetime and accounted for an obviously boosted  $NH_3$  production rate.<sup>103</sup> Similarly, Fe doped SrMoO<sub>4</sub> (Fe/Sr = 1.6) achieved a  $NH_3$  production rate of  $93.1 \mu\text{mol g}^{-1} \text{h}^{-1}$  under Xe lamp illumination.<sup>102</sup>

(2) Fe loaded onto semiconductors. Zhang *et al.* reported that Fe/TiO<sub>2-x</sub>H<sub>y</sub> could serve as a dual temperature zone catalyst for

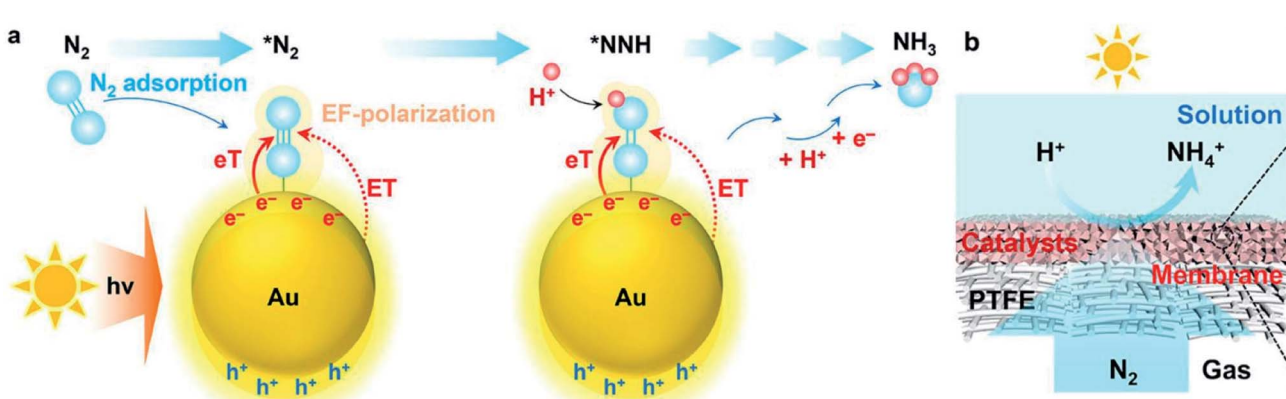


Fig. 6 (a) Schematic illustration of PNF over Uio-66 encapsulated Au nanoparticles. (b) Schematic illustration of the interface design for PNF. This figure has been adapted from ref. 94 with permission from Royal Society of Chemistry, copyright 2021.



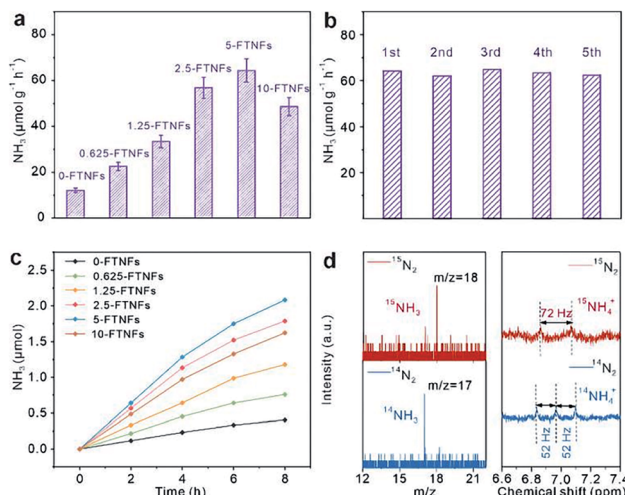


Fig. 7 (a) Performance of Fe doped TiO<sub>2</sub> (x-FTNFs, where x is the loading of Fe) in PNF. (b) Stability test of 5-FTNFs in PNF. (c) Time-dependent NH<sub>3</sub> production over x-FTNFs. (d) Isotope labeling experiment (left panel) and 1H-NMR (right panel) of the products. This figure has been adapted from ref. 99 with permission from Royal Society of Chemistry, copyright 2021.

PNF.<sup>104</sup> Under solar light irradiation, catalyst surface temperature reached 495 °C, with a temperature difference between Fe and TiO<sub>2-x</sub>H<sub>y</sub> of 137 °C, owing to the plasmonic local heating effect of Fe. Then Fe acted as the hot zone catalyst to dissociate N<sub>2</sub> via its photogenerated hot electrons, while TiO<sub>2-x</sub>H<sub>y</sub> accommodated the N atoms from Fe and hydrogenated them into NH<sub>3</sub>.<sup>104</sup> Fe/TiO<sub>2-x</sub>H<sub>y</sub> delivered a NH<sub>3</sub> concentration of 109.5 μmol g<sup>-1</sup> h<sup>-1</sup>, an order of magnitude higher than the commercial Haber-Bosch Fe catalyst.<sup>104</sup>

(3) Fe based heterostructure catalysts. Fe<sub>2</sub>O<sub>3</sub>/g-C<sub>3</sub>N<sub>4</sub> prepared by thermal treatment method exhibited a NH<sub>3</sub> production rate of 7044 μmol g<sup>-1</sup> h<sup>-1</sup> under the illumination of a 300 W Xe lamp, where the heterostructure facilitated light harvesting and Fe<sub>2</sub>O<sub>3</sub> played key roles in N<sub>2</sub> adsorption.<sup>105</sup> Oxygen deficient Fe<sub>2</sub>O<sub>3</sub>/ZnO could stably produce NH<sub>3</sub> at a rate of 80 μmol g<sup>-1</sup> h<sup>-1</sup> without any sacrificial agent under visible light irradiation.<sup>106</sup> Over Fe<sub>2</sub>O<sub>3</sub>/ZnO, the synergistic effect between oxygen vacancies and Fe<sub>2</sub>O<sub>3</sub> activated N<sub>2</sub>, while the heterostructure of Fe<sub>2</sub>O<sub>3</sub>/ZnO prohibited the recombination of electron-hole pairs, which accounted for its superior photocatalytic performance.<sup>106</sup> Fe-modified palygorskite supported FeS<sub>2</sub>, synthesized by microwave hydrothermal method, could serve as a Z scheme type photocatalysts for PNF and recorded a NH<sub>3</sub> production rate of 147 μmol g<sup>-1</sup> h<sup>-1</sup> under solar light irradiation.<sup>107</sup> Its activity was ascribed to the narrowed band gap, widened light harvesting region of Fe-modified palygorskite as well as the facilitated charge transfer between Fe-modified palygorskite and FeS<sub>2</sub>.<sup>107</sup>

(4) Other light responsive materials, such as graphdiyne and MOFs, supported Fe catalysts. For instance, Li *et al.* reported that the morphology, coordination environment and the valence state of iron oxide could be manipulated by encapsulating versatile shaped Fe<sub>3</sub>O<sub>4</sub> by graphdiyne.<sup>108</sup> The encapsulation of graphdiyne endowed Fe<sub>3</sub>O<sub>4</sub>@graphdiyne

heterojunctions strong light harvesting capacity, a structural evolution during PNF, as well as a NH<sub>3</sub> yield of an unprecedented level of ~1762 μmol g<sup>-1</sup> h<sup>-1</sup>.<sup>108</sup> The Fe atoms in Fe-based MOFs (*e.g.*, MIL-101(Fe), MIL-100(Fe), MIL-88(Fe)) have high electron densities, low reaction barriers for the activation of N<sub>2</sub> and H<sub>2</sub> to N-H bond, and could serve as the catalytic active center for PNF.<sup>109</sup> Taking MIL-101(Fe) as an example, it gave a NH<sub>3</sub> production rate of 100.7 μmol g<sup>-1</sup> h<sup>-1</sup> under the illumination of a 300 W Xe lamp.<sup>109</sup>

### Ruthenium-based catalysts for PNF

Ruthenium is another metal capable of activating N<sub>2</sub> under thermally-driven conditions. Ruthenium-based catalysts that could harvest solar light effectively have been successfully applied in PNF. Since the light harvesting capacity of ruthenium is weak, the light harvesting unit of ruthenium-based photocatalysts are generally semiconductors or other light responsive materials. Similar as iron-based catalysts, over most of the ruthenium-based catalysts for PNF, both the light harvesting unit and the active center are regulated. Based on the nature of the light responsive components, these ruthenium-based catalysts could be divided into the following categories.

(1) Semiconductor, such as TiO<sub>2</sub>, GaN, C<sub>3</sub>N<sub>4</sub> and CeO<sub>2</sub>, supported ruthenium catalysts. For example, Ru/TiO<sub>2</sub>, in which singly dispersed Ru atoms were decorated onto TiO<sub>2</sub> nanosheets rich in oxygen vacancies, is active for PNF.<sup>110</sup> Over Ru/TiO<sub>2</sub>, the single Ru atoms were possibly located at the oxygen vacancy sites and stabilized by the vacancies.<sup>110</sup> The isolated Ru atoms promoted the chemisorption of N<sub>2</sub>, boosted the electron-hole separation and overall recorded a NH<sub>3</sub> generation rate of 3.3 μmol g<sup>-1</sup> h<sup>-1</sup> upon irradiation by a 300 W high pressure Xe lamp.<sup>110</sup> Ru/P25, prepared by the facile synthetic method, exhibited Ru particle sizes of 2–3 nm. In PNF, Ru/P25 dissociated H<sub>2</sub>O to hydrogen atoms continuously and then hydrogenated N<sub>2</sub> molecules via a distal reaction pathway at the gas (N<sub>2</sub>)–liquid (H<sub>2</sub>O) interface.<sup>111</sup> The NH<sub>3</sub> yield over Ru/P25 was high up to 5.2 μmol g<sup>-1</sup> h<sup>-1</sup> under the irradiation of a Xe lamp.<sup>111</sup> GaN supported Ru catalysts, Ru/GaN, behaved tailorable electronic and morphological properties.<sup>112</sup> The interfacial Schottky junction between Ru and GaN facilitated the electron transfer from GaN to Ru, then the electron tank in Ru promoted N≡N bond dissociation and achieved NH<sub>3</sub> synthesis at low temperatures. Notably, 5 wt% Ru/GaN afforded an average NH<sub>3</sub> production rate of 120 μmol g<sup>-1</sup> h<sup>-1</sup> after 2 h UV irradiation at 10 °C (Fig. 8).<sup>112</sup>

Modifying the semiconductor supported Ru catalysts could speed up NH<sub>3</sub> production rate. For instance, modifying Ru/g-C<sub>3</sub>N<sub>4</sub> or Ru/TiO<sub>2</sub> by K could enrich the electrons in Ru, enhance the catalyst capacities in activating N<sub>2</sub> and consequently improve NH<sub>3</sub> generation rate.<sup>113,114</sup> Doping Zr<sup>4+</sup> into CeO<sub>2</sub> could increase the electron densities on Ce and create oxygen vacancies, which strengthened the interactions between Ru nanoparticles and supports.<sup>115</sup> The strong interaction upshifted the Ru d-band center relative to Fermi level and enhanced N<sub>2</sub> cleavage.<sup>115</sup> Ternary heterostructure Ru/RuO<sub>2</sub>/g-C<sub>3</sub>N<sub>4</sub> catalyst gave an average NH<sub>3</sub> production rate of 13.3 μmol g<sup>-1</sup> h<sup>-1</sup>, 6 times higher than Ru/g-C<sub>3</sub>N<sub>4</sub>.<sup>116</sup> Characterization results indicated that under light



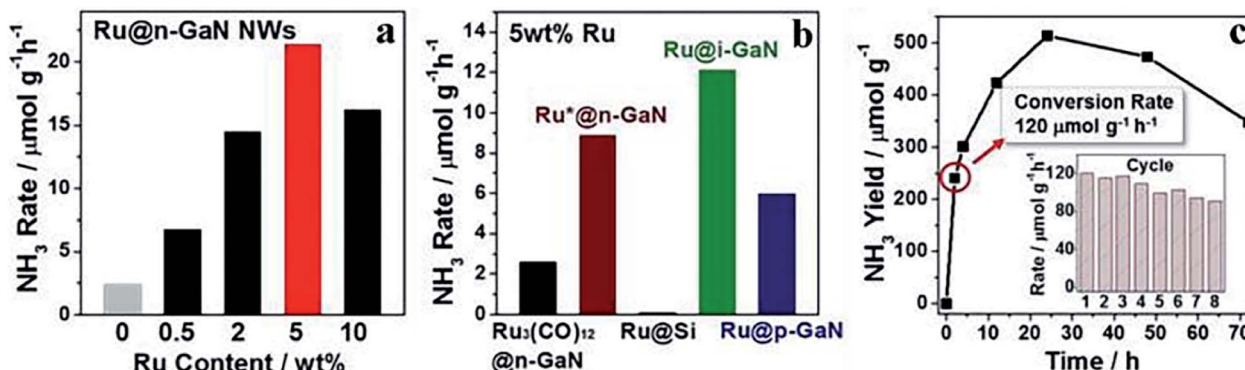


Fig. 8 NH<sub>3</sub> production rate over (a) Ru/GaN of different Ru loadings, (b) 5 wt% Ru loaded onto various supports, and (c) NH<sub>3</sub> production rate as a function of time over 5 wt% Ru/GaN under UV irradiation, with reusability of 5 wt% Ru/GaN as an inset. This figure has been adapted from ref. 112 with permission from American Chemical Society, copyright 2019.

irradiation, the electrons transferred to Ru whereas holes migrated to RuO<sub>2</sub> to facilitate the reduction and oxidation reactions, respectively, meanwhile, the electron-rich Ru activated N<sub>2</sub> effectively.<sup>116</sup> Decorating Ru/g-C<sub>3</sub>N<sub>4</sub> catalyst by S-deficient CoS<sub>x</sub> could construct a bimetallic center at the interface of Ru/CoS<sub>x</sub>, which facilitated N<sub>2</sub> polarization and activation *via* electron transfer from Ru and Co to N<sub>2</sub> upon light irradiation and ultimately gave a NH<sub>3</sub> production rate high up to 440  $\mu\text{mol g}^{-1} \text{h}^{-1}$ .<sup>117</sup>

(2) Other light responsive materials supported Ru catalysts. For example, coal-based carbon nanosheet supported Ru catalyst yielded 55.3  $\mu\text{mol g}^{-1} \text{h}^{-1}$  NH<sub>3</sub> under a 300 W Xe lamp irradiation.<sup>118</sup> Graphene oxide/silica could sufficiently disperse Ru and enhance the LSPR effect of Ru species, which excited more electron-hole pairs upon light irradiation and accelerated NH<sub>3</sub> generation.<sup>119</sup> TiO<sub>2</sub>-Mxene hybrid nanostructure supported Ru catalysts afforded an ammonia production rate of  $\sim$ 5.7  $\mu\text{mol g}^{-1} \text{h}^{-1}$ , which was principally stemmed from the synergistic effects among TiO<sub>2</sub>, Mxene and Ru.<sup>120</sup>

### Other catalysts for PNF

Numerous other catalysts have also been designed for PNF. Phosphorus is one of them. Yu *et al.* disclosed that the edges of black phosphorus (BP) could absorb and reduce N<sub>2</sub>. They synthesized an edge-rich BP nanostructure with a flake-like shape *via* chemical etching exfoliation method. The edge-rich BP is of good dispersibility in H<sub>2</sub>O, which allows its full contact with the reactants. Owing to the abundant active sites for N<sub>2</sub> chemisorption and reduction as well as the efficient contact between the reactants and catalyst, the edge-rich BP delivered a NH<sub>3</sub> production rate of 2370  $\mu\text{mol g}^{-1} \text{h}^{-1}$ .<sup>121</sup> Lin *et al.* loaded red phosphorus (RP) onto photoinactive SiO<sub>2</sub> *via* a facile sublimation-deposition method, in which RP was modified by *in situ* formed carbon.<sup>122</sup> The hybrid SiO<sub>2</sub>/C-RP catalyst was of large specific surface area, strong light harvesting capacity and high charge separation efficiency, which accounted for a NH<sub>3</sub> production rate of 36.5  $\mu\text{mol g}^{-1} \text{h}^{-1}$ .<sup>122</sup>

MOFs have also been successfully applied in PNF. Chen *et al.* unraveled that the Ce species in MOF-76(Ce) was an electron tank, which accepted photoinduced electrons to its 4f orbitals

and then donated the electrons to the anti-bonding orbitals of N<sub>2</sub>.<sup>123</sup> As a result, MOF-76(Ce) gave an average NH<sub>3</sub> yield of 34  $\mu\text{mol g}^{-1} \text{h}^{-1}$  under ambient conditions.<sup>123</sup> Ye *et al.* reported that functionalized MIL-125(Ti) could act as photocatalysts for PNF under visible light irradiation without any sacrificial reagent.<sup>124</sup> Notably, amine-functionalized NH<sub>2</sub>-MIL-125(Ti) afforded a NH<sub>3</sub> production rate of 12.3  $\mu\text{mol g}^{-1} \text{h}^{-1}$ . The electron transfer from the ligand to metal in MIL-125(Ti) induced Ti<sup>3+</sup>, which was the active sites for N<sub>2</sub> activation. Functionalization extended the light harvesting capacity of MIL-125(Ti) and further enhanced catalyst activity in PNF.<sup>124</sup>

LDH with oxygen defects and electron-rich metals have been discovered active in PNF, in which vacancies and metal centers synergistically promote N<sub>2</sub> adsorption, facilitate the separation of photoinduced electron-hole pairs, and thereby boost activity in PNF.<sup>125,126</sup> Zhang *et al.* uncovered that 0.5% mol Cu modification could impart ZnAl-LDH oxygen vacancies and electron-rich unsaturated Cu<sup>δ+</sup> ( $\delta < 2$ ).<sup>125</sup> NaOH treatment could also induce vacancies and low-coordinated metal centers in ZnCr-LDH, ZnAl-LDH and NiAl-LDH.<sup>126</sup> Taking Cu<sup>δ+</sup>-ZnAl-LDH as an example, it realized a NH<sub>3</sub> production rate of 110  $\mu\text{mol g}^{-1} \text{h}^{-1}$  under UV-vis light irradiation.<sup>125</sup>

In addition, Mo-based catalysts (*e.g.*, Mo<sub>1</sub>/g-C<sub>3</sub>N<sub>4</sub>),<sup>127</sup> carbon-tungstic-acid hybrids,<sup>128</sup> Pr<sup>3+</sup>:LiNbO<sub>3</sub>,<sup>129</sup> Pt GO/SiO<sub>2</sub> (GO: graphene oxide)<sup>130</sup> have also been utilized in PNF. These catalysts produce NH<sub>3</sub> at the magnitude of  $\mu\text{mol g}^{-1} \text{h}^{-1}$ . Meanwhile, the studies on these catalysts are quite limited and the reaction mechanism is not fully understood.

### Summary and outlooks

Ideally, PNF is a safe and green approach to synthesize NH<sub>3</sub> under ambient conditions, using the inexhaustible solar light as the sole energy input and the abundant N<sub>2</sub> as a reactant. Catalyst is the key for PNF. Over the past few years, extensive studies have been conducted to search for efficient catalysts for PNF. Semiconductor, plasmonic metal-based catalysts, iron-based catalysts, ruthenium-based catalysts and several other catalysts, have been reported active in PNF. Table 1 lists the



Table 1 The performance of some typical catalysts in PNF reaction

Catalysts	Catalytic types	Reaction conditions	NH <sub>3</sub> yield ( $\mu\text{mol g}^{-1} \text{h}^{-1}$ )	Ref.
Ultrathin MoS <sub>2</sub>	Pristine semiconductors	Water (200 mL), catalyst (15 mg), reaction temperature (25 °C), N <sub>2</sub> bubble, under light irradiation (500 W, $\lambda > 420 \text{ nm}$ , Xe lamp)	325	34
Bio quantum dots	Pristine semiconductors	Water (200 mL), catalyst (50 mg), reaction temperature (25 °C), N <sub>2</sub> bubble, under light irradiation (500 W, Xe lamp)	1226	35
PFL-g-C <sub>3</sub> N <sub>4</sub> (PFL: porous few-layer)	Defective semiconductors	20% CH <sub>3</sub> OH (100 mL), catalyst (20 mg), N <sub>2</sub> (30 min), under light irradiation (500 W, AM 1.5G, 100 mW cm <sup>-2</sup> , Xe lamp)	8200	38
D-CN (1D defective g-C <sub>3</sub> N <sub>4</sub> )	Defective semiconductors	0.1 mol L <sup>-1</sup> K <sub>2</sub> SO <sub>4</sub> solution (95 mL) and methanol (5 mL), catalyst (200 mg), reaction temperature (25 °C), N <sub>2</sub> bubble (2 h), under light irradiation (600 mW cm <sup>-2</sup> ), reaction time (8 h)	17.4	39
BOC/OV (surface oxygen vacancies modified micro-nanosheet structure Bi <sub>2</sub> O <sub>2</sub> CO <sub>3</sub> )	Defective semiconductors	0.1 mmol L <sup>-1</sup> Na <sub>2</sub> SO <sub>3</sub> solution (50 mL), catalyst (30 mg), N <sub>2</sub> (60 mL min <sup>-1</sup> , 30 min), under light irradiation (300 W, $\lambda > 420 \text{ nm}$ , Xe lamp)	14.7	40
A-SmOCl (amorphous SmOCl nanosheets)	Defective semiconductors	Water (20 mL), catalyst (10 mg), N <sub>2</sub> (30 mL min <sup>-1</sup> , 30 min), under light irradiation (250 mW cm <sup>-2</sup> , 320–780 nm, Xe lamp)	426	42
TiO <sub>2</sub> (B) nanotubes	Defective semiconductors	Mixture of water (90 mL) and methanol (10 mL), catalyst (25 mg), ultrasonic oscillation (10 min), reaction time (10 min), N <sub>2</sub> (30 min) under simulated sunlight irradiation (300 W, 60 min, AM 1.5G, Xe lamp)	106	48
TiO <sub>2</sub> -OVs (reduced TiO <sub>2</sub> )	Defective semiconductors	Mixture of water (90 mL) and methanol (10 mL), catalyst (50 mg), ultrasonic oscillation (15 min), N <sub>2</sub> (30 mL min <sup>-1</sup> ), reaction temperature (25 °C), under light irradiation (300 W, Xe lamp)	324.86	49
BCN (B-doped g-C <sub>3</sub> N <sub>4</sub> nanosheets)	Doped semiconductors	Aqueous solution of Na <sub>2</sub> SO <sub>3</sub> (40 mL, $1.0 \times 10^{-3} \text{ mol L}^{-1}$ ), catalyst (20 mg), N <sub>2</sub> (30 mL min <sup>-1</sup> , 30 min), reaction time (1 h), under light irradiation (250 W, $\lambda > 400 \text{ nm}$ , 500 mW cm <sup>-2</sup> , Xe lamp)	313.9	55
C-BiOI (carbon-doped BiOI)	Doped semiconductors	Mixture of water (90 mL) and ethanol (10 mL), catalyst (50 mg), under light irradiation (300 W, Xe lamp)	311	61
NCN/MgO (g-C <sub>3</sub> N <sub>4</sub> nanosheets decorated with MgO nanoparticles)	Functionalized semiconductors	Water (40 mL) and 40 $\mu\text{L}$ absolute ethanol (0.789 g L <sup>-1</sup> ), catalyst (40 mg), ultrasonic oscillation (6 min), N <sub>2</sub> (1 h), reaction temperature (25 °C), under light irradiation (500 W, 100 mW cm <sup>-2</sup> , $\lambda > 420 \text{ nm}$ , Xe lamp)	4554	63
KOH treated g-C <sub>3</sub> N <sub>4</sub>	Functionalized semiconductors	CH <sub>3</sub> OH (150 mL), catalyst (20 mg), reaction temperature (25 °C), under light irradiation (6 min), N <sub>2</sub> (1 h), reaction temperature (25 °C), under light irradiation (500 W, 100 mW cm <sup>-2</sup> , Xe lamp)	3632	64
Cu/TiO <sub>2</sub> (transition metal modified TiO <sub>2</sub> )	Functionalized semiconductors	5.0 vol% glycerol aqueous solution (200 mL), catalyst (100 mg), under simulating solar light irradiation (300 W, AM 1.5 filter, Xe lamp)	6780	65
P-LFO (phosphate modified LaFeO <sub>3</sub> )	Functionalized semiconductors	Water (40 mL), catalyst (20 mg), N <sub>2</sub> (1 h), under light irradiation (500 W, $\lambda > 420 \text{ nm}$ , Xe lamp)	250	72
Bi@BiOBr	Functionalized semiconductors	Water (100 mL), catalyst (10 mg), N <sub>2</sub> (80 mL min <sup>-1</sup> , 30 min), reaction temperature (15 °C), under simulating solar light irradiation (300 W, 1.63 W cm <sup>-2</sup> , Xe lamp)	1350	73
MOF@DF-C <sub>3</sub> N <sub>4</sub> (nano-MOF@defected thin film C <sub>3</sub> N <sub>4</sub> )	Heterojunctions and homojunctions	Mixture of water (48 mL) and methanol (2 mL), catalyst (10 mg), ultrasonic oscillation (15 min), reaction temperature (25 °C) under light irradiation (300 W, $\lambda > 400 \text{ nm}$ , Xe lamp)	2320	83
MoS <sub>2</sub> /C-ZnO	Heterojunctions and homojunctions	Mixture of water (190 mL) and ethanol (10 mL), catalyst (100 mg), reaction time (5 h), air, under light irradiation (300 W, $\lambda > 420 \text{ nm}$ , Xe lamp)	49.1	88
TiO <sub>2</sub> @C/g-C <sub>3</sub> N <sub>4</sub>	Heterojunctions and homojunctions	20 vol% CH <sub>3</sub> OH (100 mL), catalyst (50 mg), N <sub>2</sub> (60 mL min <sup>-1</sup> ), under light irradiation (300 W, $\lambda < 420 \text{ nm}$ , Xe lamp)	250.6	89
	Heterojunctions and homojunctions		432	92

Table 1 (Cont'd.)

Catalysts	Catalytic types	Reaction conditions	NH <sub>3</sub> yield ( $\mu\text{mol g}^{-1} \text{h}^{-1}$ )	Ref.
Na- $\text{A}_{\text{d}}/\text{R}_{\text{O}}$ (Na treatment of P25-TiO <sub>2</sub> , $\text{A}_{\text{d}}$ : Disordered anatase, $\text{R}_{\text{O}}$ : disordered rutile)	Semiconductor-based hydrophilic-hydrophobic catalyst	Water (50 mL), catalyst (50 mg), isopropyl alcohol (7 mL), N <sub>2</sub> (0.3 L min <sup>-1</sup> ) under simulated AM 1.5G sunlight irradiation (1000 W, Xe lamp) in a double-layered jacket with cooling water circulating line	16.4	93
Bi <sub>4</sub> O <sub>5</sub> Br <sub>2</sub> /ZIF-8	Plasmonic metal-based catalysts	Water (50 mL), catalyst (50 mg), N <sub>2</sub> (80 mL min <sup>-1</sup> ) under simulated sunlight irradiation (300 W, 200–800 nm, Xe lamp)	359.1	94
Au@UiO-66	Plasmonic metal-based catalysts	Aqueous solution of K <sub>2</sub> SO <sub>4</sub> (50 mL, 0.5 mol L <sup>-1</sup> ), catalyst (15 mg), N <sub>2</sub> (80 mL min <sup>-1</sup> , 30 min), reaction temperature (25 °C) under light irradiation (300 W, $\lambda > 400$ nm, 100mW cm <sup>-2</sup> , Xe lamp) in a conventional solution-based ( <i>i.e.</i> , PIS) protocol	783.4	95
Au/HCNS-NV (HCNS: Hollow mesoporous carbon nitride sphere, NV: nitrogen vacancies) Au/P25-K <sup>+</sup>	Plasmonic metal-based catalysts	Mixture of water (80 mL) and methanol (20 mL), catalyst (50 mg), ultrasonic oscillation (10 min), reaction temperature (room temperature), N <sub>2</sub> (100 mL min <sup>-1</sup> , 30 min), under light irradiation (300 W, Xe lamp)	430	98
Fe-MoTe <sub>2</sub>	Iron-based catalysts	Water (50 mL), catalyst (5 mg), N <sub>2</sub> (60 mL min <sup>-1</sup> ) under light irradiation (300 W, $\lambda > 400$ nm, 100mW cm <sup>-2</sup> , Xe lamp)	129.08	103
ML-101(Fe)	Iron-based catalysts	Milli-Q (80 mL), catalyst (10 mg), reaction temperature (25 °C), N <sub>2</sub> (50 sccm, 60 min), under light irradiation (300 W, $\lambda < 420$ nm, 400 mW cm <sup>-2</sup> , h, Xe lamp)	100.7	109
Ru-TiO <sub>2</sub>	Ruthenium-based catalysts	Water (100 mL), catalyst (50 mg), ultrasonic oscillation (10 min), reaction temperature (room temperature), N <sub>2</sub> (80 mL min <sup>-1</sup> , 30 min), under simulated light irradiation (300 W, 1 h, Xe lamp)	3.3	110
Ru-Vs-CoS/CN (Ru/CoS <sub>x</sub> with S-vacancy on graphitic carbon nitride nanosheets)	Ruthenium-based catalysts	20% ethanol solution (100 mL), catalyst (40 mg), reaction temperature (25 °C), N <sub>2</sub> (1 h), light irradiation (300 W, Xe lamp), reaction time (4 h)	438	117
SiO <sub>2</sub> /C-RP (RP: red phosphorous)	Other catalysts	10% methanol solution (50 mL), catalyst (25 mg), N <sub>2</sub> (30 min), light irradiation (300 W, 200 mW cm <sup>-2</sup> , Xe lamp)	36.5	122
Mo-PCN SACS (PNC: polymeric carbon nitride, SACS: single-atom catalysts)	Other catalysts	Water (40 mL), catalyst (20 mg), ultrasonic oscillation, N <sub>2</sub> , reaction temperature (25 °C) under light irradiation (300 W, 320 mW cm <sup>-2</sup> , Xe lamp)	830	127
Pr <sup>3+</sup> : LiNbO <sub>3</sub>	Other catalysts	Water (6 mL), catalyst (3 mg), ultrasonic oscillation (60 min), pH = 5, N <sub>2</sub> , reaction temperature (room temperature), reaction time (12 h), light irradiation (300 W, Xe lamp)	38.4	129

performances of some typical catalysts. This review summarizes the progress of each category of the catalysts designed for PNF, with a special attention on semiconductor-based catalysts. Generally speaking, the catalyst development is still in the infant stage and huge challenges need to be overcome.

(1)  $\text{NH}_3$  production rates are still low. Over most of the catalysts,  $\text{NH}_3$  production rates are in the magnitude of  $\text{mmol g}^{-1} \text{h}^{-1}$  or even  $\mu\text{mol g}^{-1} \text{h}^{-1}$ . It is far away from the industrial applications. Meanwhile, other chemicals (e.g.,  $\text{N}_2\text{H}_4$ ) are occasionally generated as byproducts. Therefore, persistent efforts should be devoted to design catalysts that could drive PNF efficiently and selectively to the desired product  $\text{NH}_3$ . Adopting novel materials as catalysts for PNF might benefit this research area.

(2) There is a long way to make clear the reaction mechanism. In spite that some studies carried out mechanism explorations, little progress have been made in understanding the fundamental mechanism. The physicochemical properties of the photocatalysts under working states remain unclear;  $\text{N}_2$  chemisorption, activation and reduction pathway on the active sites are not clarified; the electron-hole transfer and migration routes need to be understood; in-depth understanding on the structure/property–performance correlations in PNF needs to be unraveled. Theoretical studies together with *in situ* characterization techniques might offer potential approaches to make clear the reaction mechanism.

In summary, despite that the development of catalysts for PNF is still in the primary stage, progress has been made. PNF has been proved as a promising avenue to replace the industrialized Haber-Bosch process to produce  $\text{NH}_3$ . Numerous opportunities exist to move the research field forwards.

## Conflicts of interest

The authors declare no competing interests.

## Acknowledgements

This work received financial support from the National Natural Science Foundation of China (21902116), and Liaoning Revitalization Talents Program (XLYC1902070).

## References

- 1 H. Koch, M. A. H. J. van Kessel and S. Lucker, *Appl. Microbiol. Biotechnol.*, 2019, **103**, 177–189.
- 2 H. Cheng, P. Cui, F. Wang, L.-X. Ding and H. Wang, *Angew. Chem., Int. Ed.*, 2019, **58**, 15541–15547.
- 3 J. Xiong, P. Song, J. Di and H. Li, *Chem. Eng. J.*, 2020, **402**, 126208.
- 4 R. Su, Z. Liu, H. N. Abbasi, J. Wei and H. Wang, *Materials*, 2020, **13**, 4559.
- 5 K. H. R. Rouwenhorst, A. G. J. Van der Ham and L. Lefferts, *Int. J. Hydrogen Energy*, 2021, **46**, 21566–21579.
- 6 C. G. Balesdent, J. L. Crossland and D. R. Tyler, *242<sup>nd</sup> ACS National Meeting Denver*, 2011.
- 7 T. Kandemir, M. E. Schuster, A. Senyshyn, M. Behrens and R. Schloegl, *Angew. Chem., Int. Ed.*, 2013, **52**, 12723–12726.
- 8 B. A. Rohr, A. R. Singh and J. K. Norskov, *J. Catal.*, 2019, **372**, 33–38.
- 9 X. Wang, W. Wang, M. Qiao, G. Wu, W. Chen, T. Yuan, Q. Xu, M. Chen, Y. Zhang, X. Wang, J. Wang, J. Ge, X. Hong, Y. Li, Y. Wu and Y. Li, *Sci. Bull.*, 2018, **63**, 1246–1253.
- 10 J. Li, G. Zhan, J. Yang, F. Quan, C. Mao, Y. Liu, B. Wang, F. Lei, L. Li, A. W. M. Chan, L. Xu, Y. Shi, Y. Du, W. Hao, P. K. Wong, J. Wang, S.-X. Dou, L. Zhang and J. C. Yu, *J. Am. Chem. Soc.*, 2020, **142**, 7036–7046.
- 11 A. J. Medford and M. C. Hatzell, *ACS Catal.*, 2017, **7**, 2624–2643.
- 12 W. Wang, H. Zhang, S. Zhang, Y. Liu, G. Wang, C. Sun and H. Zhao, *Angew. Chem., Int. Ed.*, 2019, **58**, 16644–16650.
- 13 X. Chen, N. Li, Z. Kong, W.-J. Ong and X. Zhao, *Mater. Horiz.*, 2018, **5**, 9–27.
- 14 X. Xue, R. Chen, C. Yan, P. Zhao, Y. Hu, W. Zhang, S. Yang and Z. Jin, *Nano Res.*, 2019, **12**, 1229–1249.
- 15 M. Li, H. Huang, J. Low, C. Goo, R. Long and Y. Xiong, *Small Methods*, 2019, **3**, 1800388.
- 16 D. Yan, H. Li, C. Chen, Y. Zou and S. Wang, *Small Methods*, 2019, **3**, 1800331.
- 17 Z. Li, Z. Gao, B. Li, L. Zhang, R. Fu, Y. Li, X. Mu and L. Li, *Appl. Catal., B*, 2020, **262**, 118276.
- 18 J. Liu, M. S. Kelley, W. Wu, A. Banerjee, A. P. Douvalis, J. Wu, Y. Zhang, G. C. Schatz and M. G. Kanatzidis, *Proc. Natl. Acad. Sci. U. S. A.*, 2016, **113**, 5530–5535.
- 19 Q. Hao, C. Liu, G. Jia, Y. Wang, H. Arandian, W. Wei and B.-J. Ni, *Mater. Horiz.*, 2020, **7**, 1014–1029.
- 20 S. Chen, D. Liu and T. Peng, *Sol. RRL*, 2021, **5**, 2000487.
- 21 V. Manh-Hiep, M. Sakar and D. Trong-On, *Catalysts*, 2018, **8**, 621.
- 22 G. Zhang, C. D. Sewell, P. Zhang, H. Mi and Z. Lin, *Nano Energy*, 2020, **71**, 104645.
- 23 M.-H. Vu, M. Sakar, S. A. Hassanzadeh-Tabrizi and T.-O. Do, *Adv. Mater. Interfaces*, 2019, **6**, 1900091.
- 24 S. Zhang, Y. Zhao, R. Shi, G. I. N. Waterhouse and T. Zhang, *J. Energy Chem.*, 2019, **1**, 100013.
- 25 D. Ziegenbalg, J. Zander and R. Marschall, *Chemphotochem*, 2021, **5**, 792.
- 26 K. T. Ranjit and B. Viswanathan, *Indian Chem. Eng., Sect. A*, 1996, **35**, 443–453.
- 27 Q. Han, H. Jiao, L. Xiong and J. Tang, *Adv. Mater.*, 2021, **2**, 564.
- 28 J. Yang, *J. Chem.*, 2018, **2018**, 3286782.
- 29 Q. Han, C. Wu, H. Jiao, R. Xu, Y. Wang, J. Xie, Q. Guo and J. Tang, *Adv. Mater.*, 2021, **33**, 2008180.
- 30 G. Zhang, Y. Li, C. He, X. Ren, P. Zhang and H. Mi, *Adv. Energy Mater.*, 2021, **11**, 2003294.
- 31 M. Nazemi and M. A. El-Sayed, *Nano Energy*, 2019, **63**, 103886.
- 32 B. M. Comer and A. J. Medford, *ACS Sustainable Chem. Eng.*, 2018, **6**, 4648–4660.
- 33 G. Zhang, Y. Meng, B. Xie, Z. Ni, H. Lu and S. Xia, *Appl. Catal., B*, 2021, **296**, 120379.
- 34 S. Sun, X. Li, W. Wang, L. Zhang and X. Sun, *Appl. Catal., B*, 2017, **200**, 323–329.



35 S. Sun, Q. An, W. Wang, L. Zhang, J. Liu and W. A. Goddard III, *J. Mater. Chem. A*, 2017, **5**, 201–209.

36 Y. Liao, J. Qian, G. Xie, Q. Han, W. Dang, Y. Wang, L. Lv, S. Zhao, L. Luo, W. Zhang, H.-Y. Jiang and J. Tang, *Appl. Catal., B*, 2020, **273**, 119054.

37 Z.-K. Shen, Y.-J. Yuan, P. Wang, W. Bai, L. Pei, S. Wu, Z.-T. Yu and Z. Zou, *ACS Appl. Mater. Interfaces*, 2020, **12**, 17343–17352.

38 Y. Xue, X. Kong, Y. Guo, Z. Liang, H. Cui and J. Tian, *J. Materiomics*, 2020, **6**, 128–137.

39 D. Hao, C. Liu, X. Xu, M. Kianinia, I. Aharonovich, X. Bai, X. Liu, Z. Chen, W. Wei, G. Jia and B.-J. Ni, *New J. Chem.*, 2020, **44**, 20651–20658.

40 Y. Feng, Z. Zhang, K. Zhao, S. Lin, H. Li and X. Gao, *J. Colloid Interface Sci.*, 2021, **583**, 499–509.

41 Y. Zhao, E. Wang and R. Jin, *Diamond Relat. Mater.*, 2019, **94**, 146–154.

42 T. Hou, R. Guo, L. Chen, Y. Xie, J. Guo, W. Zhang, X. Zheng, W. Zhu, X. Tan and L. Wang, *Nano Energy*, 2019, **65**, 104003.

43 Y. Li, X. Chen, M. Zhang, Y. Zhu, W. Ren, Z. Mei, M. Gu and F. Pan, *Catal. Sci. Technol.*, 2019, **9**, 803–810.

44 S. Wang, X. Hai, X. Ding, K. Chang, Y. Xiang, X. Meng, Z. Yang, H. Chen and J. Ye, *Adv. Mater.*, 2017, **29**, 1701774.

45 H. Han, Y. Yang, J. Liu, X. Zheng, X. Wang, S. Meng, S. Zhang, X. Fu and S. Chen, *ACS Appl. Energy Mater.*, 2020, **3**, 11275–11284.

46 T. Wang, C. Feng, J. Liu, D. Wang, H. Hu, J. Hu, Z. Chen and G. Xue, *Chem. Eng. J.*, 2021, **414**, 128827.

47 Y. Shiraishi, M. Hashimoto, K. Chishiro, K. Moriyama, S. Tanaka and T. Hirai, *J. Am. Chem. Soc.*, 2020, **142**, 7574–7583.

48 S. Wu, X. Tan, K. Liu, J. Lei, L. Wang and J. Zhang, *Catal. Today*, 2019, **335**, 214–220.

49 G. Zhang, X. Yang, C. He, P. Zhang and H. Mi, *J. Mater. Chem. A*, 2020, **8**, 334–341.

50 Y. Zhang, X. Chen, S. Zhang, L. Yin and Y. Yang, *Chem. Eng. J.*, 2020, **401**, 126033.

51 X. Xue, R. Chen, H. Chen, Y. Hu, Q. Ding, Z. Liu, L. Ma, G. Zhu, W. Zhang, Q. Yu, J. Liu, J. Ma and Z. Jin, *Nano Lett.*, 2018, **18**, 7372–7377.

52 B. Liu, A. S. Yasin, T. Musho, J. Bright, H. Tang, L. Huang and N. Wu, *J. Electrochem. Soc.*, 2019, **166**, H3091–H3096.

53 Y. Zhao, Y. Zhao, R. Shi, B. Wang, G. I. N. Waterhouse, L.-Z. Wu, C.-H. Tung and T. Zhang, *Adv. Mater.*, 2019, **31**, 1806482.

54 J. Qin, W. Zhao, X. Hu, J. Li, P. Ndokoye and B. Liu, *ACS Appl. Mater. Interfaces*, 2021, **13**, 7127–7134.

55 W. Wang, H. Zhou, Y. Liu, S. Zhang, Y. Zhang, G. Wang, H. Zhang and H. Zhao, *Small*, 2020, **16**, 1906880.

56 Z. Ying, S. Chen, S. Zhang, T. Peng and R. Li, *Appl. Catal., B*, 2019, **254**, 351–359.

57 X. Xue, H. Chen, Y. Xiong, R. Chen, M. Jiang, G. Fu, Z. Xi, X. L. Zhang, J. Ma, W. Fang and Z. Jin, *ACS Appl. Mater. Interfaces*, 2021, **13**, 4975–4983.

58 D. Wu, R. Wang, C. Yang, Y. An, H. Lu, H. Wang, K. Cao, Z. Gao, W. Zhang, F. Xu and K. Jiang, *J. Colloid Interface Sci.*, 2019, **556**, 111–119.

59 J. Li, D. Wang, R. Guan, Y. Zhang, Z. Zhao, H. Zhai and Z. Sun, *ACS Sustainable Chem. Eng.*, 2020, **8**, 18258–18265.

60 S. Cao, B. Fan, Y. Feng, H. Chen, F. Jiang and X. Wang, *Chem. Eng. J.*, 2018, **353**, 147–156.

61 L. Zeng, F. Zhe, Y. Wang, Q. Zhang, X. Zhao, X. Hu, Y. Wu and Y. He, *J. Colloid Interface Sci.*, 2019, **539**, 563–574.

62 P. Qiu, Z. Liang, X. Liu, X. Qian, H. Cui and J. Tian, *J. Colloid Interface Sci.*, 2020, **571**, 318–325.

63 E. Vesali-Kermani, A. Habibi-Yangjeh and S. Ghosh, *J. Ind. Eng. Chem.*, 2020, **84**, 185–195.

64 X. Li, X. Sun, L. Zhang, S. Sun and W. Wang, *J. Mater. Chem. A*, 2018, **6**, 3005–3011.

65 Y. Liu, Z. Yu, S. Guo, L. Yao, R. Sun, X. Huang and W. Zhao, *New J. Chem.*, 2020, **44**, 19924–19932.

66 J. M. Walls, J. S. Sagu and K. G. U. Wijayantha, *RSC Adv.*, 2019, **9**, 6387–6394.

67 T. Fei, L. Yu, Z. Liu, Y. Song, F. Xu, Z. Mo, C. Liu, J. Deng, H. Ji, M. Cheng, Y. Lei, H. Xu and H. Li, *J. Colloid Interface Sci.*, 2019, **557**, 498–505.

68 Y. Hao, X. Dong, S. Zhai, H. Ma, X. Wang and X. Zhang, *Chem.-Eur. J.*, 2016, **22**, 18722–18728.

69 S. Cao, H. Chen, F. Jiang and X. Wang, *Appl. Catal., B*, 2018, **224**, 222–229.

70 Y. Kong, C. Lv, C. Zhang and G. Chen, *Appl. Surf. Sci.*, 2020, **515**, 146009.

71 Y. Bi, Y. Wang, X. Dong, N. Zheng, H. Ma and X. Zhang, *RSC Adv.*, 2018, **8**, 21871–21878.

72 X. Sun, D. Jiang, L. Zhang, S. Sun and W. Wang, *ACS Sustainable Chem. Eng.*, 2017, **5**, 9965–9971.

73 M. Lan, N. Zheng, X. Dong, H. Ma and X. Zhang, *Colloids Surf., A*, 2021, **623**, 126744.

74 X. Rong, Y. Mao, J. Xu, X. Zhang, L. Zhang, X. Zhou, F. Qiu and Z. Wu, *Catal. Commun.*, 2018, **116**, 16–19.

75 H. Mou, J. Wang, D. Yu, D. Zhang, W. Chen, Y. Wang, D. Wang and T. Mu, *ACS Appl. Mater. Interfaces*, 2019, **11**, 44360–44365.

76 C. Xiao, H. Wang, L. Zhang, S. Sun and W. Wang, *Chemcatchem*, 2019, **11**, 6467–6472.

77 H. Zhang, X. Li, H. Su, X. Chen, S. Zuo, X. Yan, W. Liu and C. Yao, *J. Sol-Gel Sci. Technol.*, 2019, **92**, 154–162.

78 G. Zhang, T. Dai, Y. Wang, Y. Meng, B. Xie, Z. Ni and S. Xia, *Appl. Catal., B*, 2021, **288**, 119990.

79 Y. Chen, C. Zhao, S. Ma, P. Xing, X. Hu, Y. Wu and Y. He, *Inorg. Chem. Front.*, 2019, **6**, 3083–3092.

80 S. Xia, G. Zhang, Z. Gao, Y. Meng, B. Xie, H. Lu and Z. Ni, *J. Colloid Interface Sci.*, 2021, **604**, 798–809.

81 S. Cao, N. Zhou, F. Gao, H. Chen and F. Jiang, *Appl. Catal., B*, 2017, **218**, 600–610.

82 Y. Wang, W. Wei, M. Li, S. Hu, J. Zhang and R. Feng, *RSC Adv.*, 2017, **7**, 18099–18107.

83 Z. Ding, S. Wang, X. Chang, D.-H. Wang and T. Zhang, *RSC Adv.*, 2020, **10**, 26246–26255.

84 T. Wang, J. Liu, P. Wu, C. Feng, D. Wang, H. Hu and G. Xue, *J. Mater. Chem. A*, 2020, **8**, 16590–16598.

85 H. Liang, L. Fang and S. Hu, *New J. Chem.*, 2019, **43**, 12094–12102.



86 W. Guang, Y. Lihua, L. Yifu, Z. Jiaming, H. Zheng and G. Gui, *Appl. Surf. Sci.*, 2019, **481**, 649–660.

87 X. Xue, R. Chen, C. Yan, Y. Hu, W. Zhang, S. Yang, L. Ma, G. Zhu and Z. Jin, *Nanoscale*, 2019, **11**, 10439–10445.

88 P. Xing, P. Chen, Z. Chen, X. Hu, H. Lin, Y. Wu, L. Zhao and Y. He, *ACS Sustainable Chem. Eng.*, 2018, **6**, 14866–14879.

89 Q. Liu, L. Ai and J. Jiang, *J. Mater. Chem. A*, 2018, **6**, 4102–4110.

90 Y. Shiraishi, K. Chishiro, S. Tanaka and T. Hirai, *Langmuir*, 2020, **36**, 734–741.

91 H. Xu, Y. Wang, X. Dong, N. Zheng, H. Ma and X. Zhang, *Appl. Catal., B*, 2019, **257**, 117932.

92 J. Lee, X. Liu, A. Kumar, Y. Hwang, E. Lee, J. Yu, Y. D. Kim and H. Lee, *Chem. Sci.*, 2021, **12**, 9619–9629.

93 J. Liu, R. Li, X. Zu, X. Zhang, Y. Wang, Y. Wang and C. Fan, *Chem. Eng. J.*, 2019, **371**, 796–803.

94 L.-W. Chen, Y.-C. Hao, Y. Guo, Q. Zhang, J. Li, W.-Y. Gao, L. Ren, X. Su, L. Hu, N. Zhang, S. Li, X. Feng, L. Gu, Y.-W. Zhang, A.-X. Yin and B. Wang, *J. Am. Chem. Soc.*, 2021, **143**, 5727–5736.

95 Y. Guo, J. Yang, D. Wu, H. Bai, Z. Yang, J. Wang and B. Yang, *J. Mater. Chem. A*, 2020, **8**, 16218–16231.

96 Y. Wang, R. Zhao, F. Wang, Y. Liu, X. Yu, L. Chen, Y. Yao, S. Lu and X. Liao, *Catal. Sci. Technol.*, 2020, **10**, 7652–7660.

97 P. Qiu, C. Huang, G. Dong, F. Chen, F. Zhao, Y. Yu, X. Liu, Z. Li and Y. Wang, *J. Mater. Chem. A*, 2021, **9**, 14459–14465.

98 T.-A. Bu, Y.-C. Hao, W.-Y. Gao, X. Su, L.-W. Chen, N. Zhang and A.-X. Yin, *Nanoscale*, 2019, **11**, 10072–10079.

99 Y. Bo, H. Wang, Y. Lin, T. Yang, R. Ye, Y. Li, C. Hu, P. Du, Y. Hu, Z. Liu, R. Long, C. Gao, B. Ye, L. Song, X. Wu and Y. Xiong, *Angew. Chem., Int. Ed.*, 2021, **60**, 16085–16092.

100 X. Chen, X. Zhang, Y.-H. Li, M.-Y. Qi, J.-Y. Li, Z.-R. Tang, Z. Zhou and Y.-J. Xu, *Appl. Catal., B*, 2021, **281**, 119516.

101 Z. Ying, S. Chen, T. Peng, R. Li and J. Zhang, *Eur. J. Inorg. Chem.*, 2019, **2019**, 2182–2192.

102 J. Luo, X. Bai, Q. Li, X. Yu, C. Li, Z. Wang, W. Wu, Y. Liang, Z. Zhao and H. Liu, *Nano Energy*, 2019, **66**, 104187.

103 H. Li, S. Gu, Z. Sun, F. Guo, Y. Xie, B. Tao, X. He, W. Zhang and H. Chang, *J. Mater. Chem. A*, 2020, **8**, 13038–13048.

104 C. Mao, H. Li, H. Gu, J. Wang, Y. Zou, G. Qi, J. Xu, F. Deng, W. Shen, J. Li, S. Liu, J. Zhao and L. Zhang, *Chem.*, 2019, **5**, 2702–2717.

105 S. Liu, S. Wang, Y. Jiang, Z. Zhao, G. Jiang and Z. Sun, *Chem. Eng. J.*, 2019, **373**, 572–579.

106 Q. Chen, Y. Zhou, J.-X. Zhu, T.-T. Liang, R.-B. Huang and A.-M. Chen, *Chin. J. Inorg. Chem.*, 2020, **36**, 426–434.

107 X. Ye, X. Li, X. Chu, Z. Wang, S. Zuo, T. Wang and C. Yao, *J. Alloys Compd.*, 2021, **871**, 159542.

108 Y. Fang, Y. Xue, L. Hui, H. Yu and Y. Li, *Angew. Chem., Int. Ed.*, 2021, **60**, 3170–3174.

109 G. Li, F. Li, J. Liu and C. Fan, *J. Solid State Chem.*, 2020, **285**, 121245.

110 S. Liu, Y. Wang, S. Wang, M. You, S. Hong, T.-S. Wu, Y.-L. Soo, Z. Zhao, G. Jiang, J. Qiu, B. Wang and Z. Sun, *ACS Sustainable Chem. Eng.*, 2019, **7**, 6813–6820.

111 Y. Liao, J. Lin, B. Cui, G. Xie and S. Hu, *J. Photochem. Photobiol., A*, 2020, **387**, 112100.

112 L. Li, Y. Wang, S. Vanka, X. Mu, Z. Mi and C.-J. Li, *Angew. Chem., Int. Ed.*, 2017, **56**, 8701–8705.

113 H. Liu, P. Wu, H. Li, Z. Chen, L. Wang, X. Zeng, Y. Zhu, Y. Jiang, X. Liao, B. S. Haynes, J. Ye, C. Stampfl and J. Huang, *Appl. Catal., B*, 2019, **259**, 118026.

114 C. Mao, L. Yu, J. Li, J. Zhao and L. Zhang, *Appl. Catal., B*, 2018, **224**, 612–620.

115 Z. Ma, X. Xiong, C. Song, B. Hu and W. Zhang, *RSC Adv.*, 2016, **6**, 51106–51110.

116 H. Wang, X. Li, Q. Ruan and J. Tang, *Nanoscale*, 2020, **12**, 12329–12335.

117 Y. Jili, Y. Xuanying, T. Yanhong, L. Meijun and L. Chengbin, *Adv. Funct. Mater.*, 2020, **30**, 1906983.

118 A. Awati, H. Maimaiti, S. Wang and B. Xu, *Sci. Total Environ.*, 2019, **695**, 133865.

119 H. Maimaiti, S. Wang, A. Awati and B. Xu, *J. Nanopart. Res.*, 2020, **22**, 101.

120 C. Hao, Y. Liao, Y. Wu, Y. An, J. Lin, Z. Gu, M. Jiang, S. Hu and X. Wang, *J. Phys. Chem. Solids*, 2020, **136**, 109141.

121 S. Bian, M. Wen, J. Wang, N. Yang, P. K. Chu and X.-F. Yu, *J. Phys. Chem. Lett.*, 2020, **11**, 1052–1058.

122 L. Lin, Q. Zhu, A. Cheng and L. Ma, *Catal. Sci. Technol.*, 2020, **10**, 4119–4125.

123 C. Zhang, Y. Xu, C. Lv, X. Zhou, Y. Wang, W. Xing, Q. Meng, Y. Kong and G. Chen, *ACS Appl. Mater. Interfaces*, 2019, **11**, 29917–29923.

124 H. Huang, X.-S. Wang, D. Philo, F. Ichihara, H. Song, Y. Li, D. Li, T. Qiu, S. Wang and J. Ye, *Appl. Catal., B*, 2020, **267**, 118686.

125 S. Zhang, Y. Zhao, R. Shi, C. Zhou, G. I. N. Waterhouse, L.-Z. Wu, C.-H. Tung and T. Zhang, *Adv. Energy Mater.*, 2020, **10**, 1901973.

126 Y. Zhao, L. Zheng, R. Shi, S. Zhang, X. Bian, F. Wu, X. Cao, G. I. N. Waterhouse and T. Zhang, *Adv. Energy Mater.*, 2020, **10**, 2002199.

127 X.-W. Guo, S.-M. Chen, H.-J. Wang, Z.-M. Zhang, H. Lin, L. Song and T.-B. Lu, *J. Mater. Chem. A*, 2019, **7**, 19831–19837.

128 X. Li, W. Wang, D. Jiang, S. Sun, L. Zhang and X. Sun, *Chem.-Eur. J.*, 2016, **22**, 13819–13822.

129 L. Sun, X. Chu, C. He, S. Zuo, X. Li and C. Yao, *Appl. Phys. A: Mater. Sci. Process.*, 2021, **127**, 35.

130 B. Xu, H. Maimaiti, S. Wang, P. Zhai and H. Zhang, *React. Kinet., Mech. Catal.*, 2020, **130**, 1155–1170.

